

## Statistical modeling of the effect of chemical inhomogeneity on incipient plasticity in complex concentrated alloys

Anne Marie Z. Tan <sup>1,2,\*</sup>, Zhi Li <sup>1</sup> and Huajian Gao <sup>2,1</sup>

<sup>1</sup>*Institute of High Performance Computing (IHPC), Agency for Science, Technology and Research (A\*STAR), 1 Fusionopolis Way, #16-16 Connexis, Singapore 138632, Republic of Singapore*

<sup>2</sup>*School of Mechanical and Aerospace Engineering, Nanyang Technological University, Singapore 639798, Republic of Singapore*



(Received 13 February 2023; accepted 18 April 2023; published 2 May 2023)

In recent years, complex concentrated alloys (CCAs), also referred to as medium- or high-entropy alloys, have attracted substantial research interest due to their excellent mechanical properties including high strength, ductility, and toughness. It is known that the chemical inhomogeneity of CCAs gives rise to spatial variations in local properties such as the generalized stacking fault energy (GSFE) surface, which in turn affect their mechanical properties, but how such an inhomogeneity affects dislocation nucleation and incipient plasticity remains largely unknown and unexplored. Here, we develop a physics-informed statistical model for incipient plasticity in CCAs by combining elasticity theory for dislocation nucleation and statistical modeling of nanoindentation. Our model connects a material's fundamental properties to the statistics of incipient plasticity and is validated by the excellent agreement with the statistical data from molecular dynamics simulations of nanoindentation of CrCoNi CCA samples. By accounting for the spatial variation in the local generalized stacking fault energy surface in CCAs, our model captures the key difference in the nanoindentation-induced incipient plasticity response of CCAs compared with a conventional metal (fcc Cu) and also reproduces the trends across CCA samples with different degrees of short-range ordering. Our model also reveals a critical length scale for the underlying GSFE fluctuations which controls the overall statistics of incipient plasticity during nanoindentation of CCAs, which reflects the critical loop size of the underlying dislocation nucleation mechanism.

DOI: [10.1103/PhysRevMaterials.7.053601](https://doi.org/10.1103/PhysRevMaterials.7.053601)

### I. INTRODUCTION

Complex concentrated alloys (CCAs), which include high-entropy alloys and their derivatives, medium-entropy alloys, have attracted substantial research interest due to their potential as a new class of metallic structural materials with superior mechanical properties [1–3]. Typically comprising three to five principal elements in roughly equiatomic ratios forming a single-phase solid solution, CCAs were originally conceived to be completely random in order to maximize configurational entropy (hence the name “high-entropy alloys”) [4]. However, detailed microscopy [5,6] and first-principles calculations [7–9] have since shown that significant chemical short-range ordering (SRO) can and often does exist in CCAs at the local level. Many CCAs—including the original high-entropy alloy CrMnFeCoNi (Cantor alloy) [10] and one of its derivatives, the medium-entropy alloy CrCoNi—have demonstrated excellent mechanical properties, including high tensile strength, ductility, and toughness, as well as potential resistance to hydrogen embrittlement [11–14]. This has motivated active research in the area of CCAs in order to better understand the mechanisms underlying their desirable mechanical properties and provide insights into how to tailor new alloys with even more superior properties.

In recent years, there have been some efforts to understand the mechanisms underlying the mechanical behavior of CCAs and the role played by the chemical short-range ordering (SRO) in these processes via atomistic simulations and modeling. Some earlier efforts in atomistic modeling of plasticity in high-entropy alloys have been reviewed by Aitken *et al.* [15], while some of the unusual features of dislocations and their slip behavior in CCAs are summarized by Ma [16]. Density functional theory (DFT) calculations [8] have shown that the intrinsic and extrinsic stacking fault energies in CrCoNi CCA vary significantly with the degree of SRO, increasing from negative values in the random solid solution to positive values in samples with high SRO. Li *et al.* [17] developed an empirical embedded-atom method (EAM) potential for CrCoNi which demonstrates the spatial variation in planar fault energies in samples with different degrees of SRO, and using atomistic molecular dynamics (MD) simulations, they showed that the rugged energy landscape leads to a wavy dislocation line and dislocation glide via a “jerky” nanoscale segment detrapping mechanism. MD simulations can also provide insight into the interaction between twin boundaries and dislocations during deformation [18], competition between multiple deformation mechanisms [19], and dislocation glide mechanisms in non-fcc CCAs [20,21]. The strengthening effect of SRO and fluctuations in the generalized stacking fault energy (GSFE) landscape on dislocation glide has also been modeled at higher length scales, for example, within phase field dislocation dynamics [22],

\*anne\_marie\_tan\_zhao\_hui@ihpc.a-star.edu.sg

stochastic Peierls-Nabarro models [23], and a crystal plasticity model [24].

While most of the studies have looked at the effect of SRO on plasticity via dislocation glide, fewer studies have focused on the processes governing incipient plasticity in CCAs, i.e., dislocation nucleation. DFT and MD simulations of CrCoNi by Cao *et al.* [25] found that upon uniaxial compression, dislocations nucleated preferentially at energetically unstable bcc-like defect clusters in regions of weak Cr-Cr bonding. Xiao *et al.* [26] performed MD simulations of dislocation nucleation in CoNiCrFeMn and reported that the low stacking fault energy (SFE) leads to lower activation energy and activation volume but higher athermal stress for dislocation nucleation compared with conventional metals. Jian *et al.* [27] also performed MD simulations to investigate the roles of chemical SRO and lattice distortion in dislocation nucleation and propagation in CrCoNi.

Experimentally, incipient plasticity in various CCAs has been probed via nanoindentation [28–30]. However, such experiments do have limitations: It is difficult to identify the dislocation nucleation mechanisms activated in each case and practically impossible to isolate specific mechanisms for detailed analysis. This is where MD simulations have been able to provide further insights into the different atomistic processes occurring during nanoindentation of metals [31–34], ordered intermetallics [35–37], and, in recent years, even CCAs [38–43]. These studies have demonstrated the formation and evolution of dislocation loops and complex structures such as locks, have demonstrated the effect of crystal anisotropy, surface orientation, and microstructural elements such as nanotwins, and can be used to generate statistical distributions of pop-in loads similar to experiments. Schuh, Lund, and Mason [44–46] developed a statistical model of incipient plasticity during nanoindentation, which assumes a simple empirical form of the rate equation for activation of the dislocation nucleation process. This statistical approach has been applied to experimental data but not to analyzing data from simulations. Furthermore, such a model would not be able to explicitly account for the effect of the spatially varying properties in CCAs, or the length scale of such fluctuations, which we believe are important parameters that influence the statistics of nanoindentation-induced incipient plasticity in CCAs.

In this paper, we have developed a physics-informed statistical model which connects a material’s fundamental properties—and the spatial variations thereof—to the statistics of incipient plasticity during nanoindentation and validated the model against statistical data obtained from MD nanoindentation simulations on fcc Cu and CrCoNi alloys. To simplify the problem, we consider nanoindentation of defect-free, single-crystal CCA samples in which dislocations nucleate homogeneously from the bulk rather than heterogeneously from preexisting defects. The details of the corresponding MD simulations are described in Sec. II A, while the statistical models for nanoindentation-induced incipient plasticity in conventional metals and CCAs are derived in Secs. II B 1 and II B 2, respectively. The results presented in Sec. III demonstrate that by accounting for the spatial variation in the local generalized stacking fault energy surface arising from the chemical inhomogeneity of CCAs, our model

captures the key difference in the response of CCAs compared with a conventional metal (fcc Cu) and also reproduces the trends across CCA samples with different degrees of SRO. We provide further interpretation of our results and discuss some of their wider implications in Sec. IV. Our model highlights that the critical length scale of the underlying GSFE fluctuations, which controls the overall statistics of incipient plasticity during nanoindentation of CCAs, is closely related to the critical length scale of the dislocation nucleation mechanism.

## II. METHODOLOGY

### A. Molecular dynamics simulations

MD simulations were performed using the large-scale atomic/molecular massively parallel simulator (LAMMPS) [47] with embedded-atom method (EAM) interatomic potentials for pure Cu [48] and equiatomic CrCoNi alloys with varying degrees of SRO [17]. The dimensions of the samples in our simulations are around  $20 \times 20 \times 12$  nm, and the samples contain approximately  $0.5 \times 10^6$  atoms each. Random solid solution (RSS) CrCoNi samples were created by randomly replacing two-thirds of the Ni atoms in a face-centered cubic (fcc) Ni sample with an equal number of Co and Cr atoms. RSS samples were subsequently annealed through hybrid molecular dynamics and Monte Carlo simulations under the variance-constrained semi-grand-canonical ensemble [49] at 600 and 900 K, respectively, to obtain samples with high and low SRO. The variance constraint parameter was set as 1000 in our simulations, and 400 000 integration steps were used to generate equilibrium configurations at each given temperature. Three representative samples were created from different initial RSS alloys for each selected temperature. The degree of the chemical short-range order in the annealed samples was characterized by a pairwise order parameter [17],

$$\alpha_{ij} = \frac{p_{ij} - C_j}{\delta_{ij} - C_j}, \quad (1)$$

where  $p_{ij}$  is the probability of finding a  $j$ -type atom in the first-nearest-neighbor shell of  $i$ -type atoms,  $C_j$  is the nominal concentration of  $j$ -type atoms, and  $\delta_{ij}$  is the Kronecker delta function. For pairs of different species (i.e.,  $i \neq j$ ), a negative  $\alpha_{ij}$  suggests a tendency for  $i$ - $j$  clustering, while clustering between pairs of the same species (i.e.,  $i = j$ ) is indicated by a positive  $\alpha_{ij}$ .

The above samples were indented on the (111) surface as shown in Fig. 1(b) by a virtual rigid spherical indenter with a radius of 6 nm at the velocity of 3.5 m/s to study the effects of local SRO on the incipient plasticity. Periodic boundary conditions were applied in the  $[11\bar{2}]$  and  $[1\bar{1}0]$  directions, while the free surface boundary condition was applied in the indentation direction. The samples were equilibrated at 300 K for 300 ps before indentation using an isothermal-isobaric ( $N$ - $P$ - $T$ ) ensemble with zero pressure in the  $[11\bar{2}]$  and  $[1\bar{1}0]$  directions. During the nanoindentation process, the rigid spherical indenter exerted a repulsive force of magnitude  $K(r - R)^2$  when the distance,  $r$ , between the atom and the center of the indenter was smaller than the radius of the indenter  $R$ . The coefficient  $K$  was set at 10 eV/Å in our simulations. The bottom few layers (1.5 nm) of the simulation

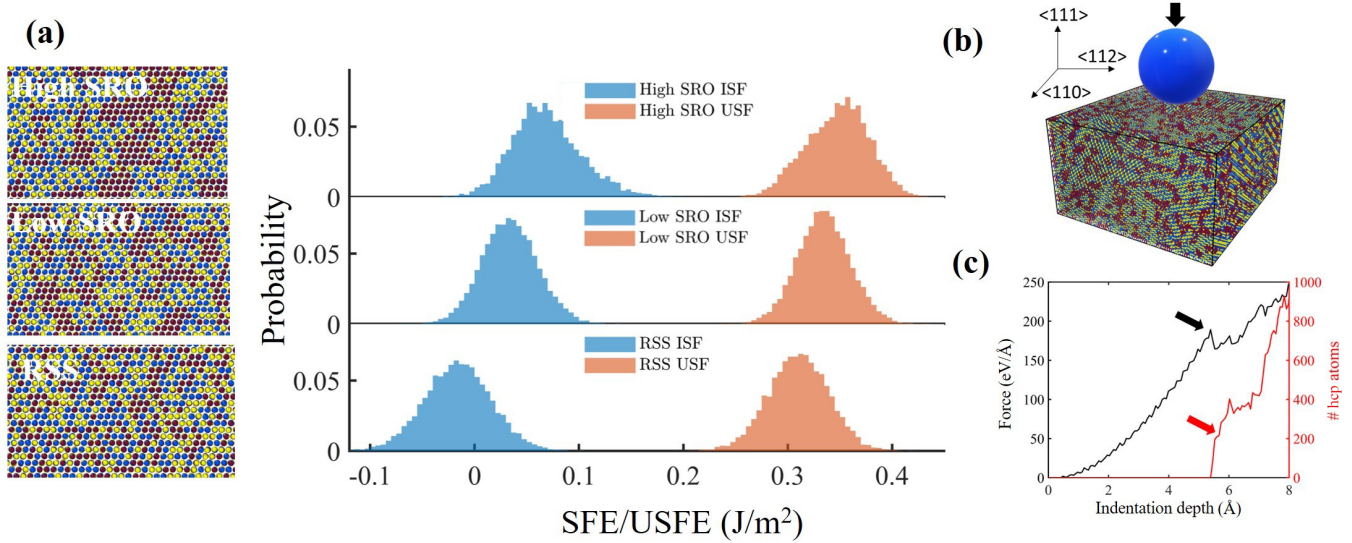


FIG. 1. (a) Distribution of local intrinsic stacking fault energy (ISFE) and unstable stacking fault energy (USFE) for three CrCoNi samples with different degree of Cr-Co ordering. (b) A typical CrCoNi sample with dimensions of  $20 \times 20 \times 10$  nm indented by a spherical indenter with a radius of 6 nm. (c) Load and structure evolution of a typical sample during indentation. The abrupt increase in the number of hcp atoms in the sample indicates dislocation nucleation.

cell were treated as the boundary layer and fixed during the nanoindentation. The next few layers (1.5 nm) adjacent to the boundary layer were set as a thermostat layer where the canonical ( $N$ - $V$ - $T$ ) ensemble was adopted, and the temperature was kept constant at 300 K. The microcanonical ensemble ( $N$ - $V$ - $E$ ) was used for the rest of the sample. A similar simulation setup has been adopted in the literature to investigate the dislocation nucleation in nanoindentation for pure metal and CCAs [34,43]. The total force on the indenter and the indentation depth were recorded during each simulation. The first significant load-drop event (corresponding to the first pop-in event in nanoindentation experiments) indicates the onset of dislocation nucleation, and the corresponding indentation force was used to calculate the incipient strength. To obtain a statistical representation of the incipient strength, 90 individual nanoindentation tests were performed for each of the pure Cu and different CrCoNi alloys, respectively. The contact surfaces between the indenter and the test samples were shifted randomly among different indentation tests to introduce different local chemical environments under the indenter.

The statistical distributions of local stacking fault energy (SFE) and unstable stacking fault energy (USFE) are two key input parameters for the theoretical model and were calculated with a resolution of  $1.6 \times 1.6$  nm. The whole sample was divided into columns with the same cross-sectional area of around  $1.6 \times 1.6$  nm at the slip plane and displaced for  $a\sqrt{6}/2$  along the [112] direction, where  $a$  is the lattice parameter. The local SFE and USFE were obtained by calculating the change in the potential energy of each column after the displacement and dividing it by the unit surface area. For each type of CrCoNi alloy with SRO, the distributions of SFE and USFE were obtained from 30 different slip planes in three individual annealed samples.

## B. Model development

### 1. Model I: Conventional metal

We first combine the homogeneous dislocation nucleation model developed by Aubry *et al.* [50] with Schuh, Lund, and Mason's statistical model of incipient plasticity during nanoindentation [44–46], to develop a model to describe the statistics of incipient plasticity driven by homogeneous dislocation nucleation during nanoindentation of a pure metal. By replacing the empirical expression for the nucleation energy barrier in Schuh, Lund, and Mason's model with an expression for homogeneous dislocation nucleation derived from elasticity theory, we are able to more explicitly and quantitatively connect the statistical behavior of the material to the underlying physical mechanism and fundamental material properties. In the following section, we will then modify the model to describe these statistics in a random complex concentrated alloy (CCA) by accounting for the spatial variation in mechanical properties present in such alloys.

Following Aubry *et al.* [50], we consider the homogeneous nucleation of a Shockley partial dislocation with Burgers vector  $\vec{b}_p = \langle 112 \rangle / 6$  on the {111} plane. In a defect-free crystal, dislocations nucleate homogeneously via the formation of a dislocation loop bounding a stacking fault; hence the energetics of this process involves the elastic energy of the dislocation, the stacking fault energy, and the work done by an applied shear stress.

In the simplest model, the magnitude of the Burgers vector is assumed to be a constant  $b = |\vec{b}_p|$ , such that the energy of a circular dislocation loop is given by [50]

$$E(R; \tau_{\text{res}}) = 2\pi R \frac{\mu b^2}{8\pi} \left[ \frac{2-v}{1-v} \left( \ln \frac{8R}{r_{\text{cut}}} - 2 \right) + \frac{1}{2} \right] + \gamma_{\text{SF}} \pi R^2 - b \tau_{\text{res}} \pi R^2, \quad (2)$$

where  $R$  is the radius of the dislocation loop,  $r_{\text{cut}}$  is the dislocation core cutoff radius, and  $\mu$ ,  $\nu$ , and  $\gamma_{\text{ISF}}$  are the shear modulus, Poisson ratio, and intrinsic stacking fault energy of the system, respectively.  $\tau_{\text{res}}$  is the resolved shear stress on the slip plane of interest, which is related to the applied shear stress  $\tau_{\text{appl}}$  by the Schmid factor  $m$ ,  $\tau_{\text{res}} = m\tau_{\text{appl}}$ . In this paper, we chose  $r_{\text{cut}} = 1.0b$ . The energy barrier for dislocation nucleation at a given  $\tau_{\text{res}}$  is determined by the maximum of Eq. (2).

By allowing the magnitude of the Burgers vector to be a variable  $b_f$ , the energy of the dislocation loop may instead be written as

$$E(b_f, R; \tau_{\text{res}}) = 2\pi R \frac{\mu b_f^2}{8\pi} \left[ \frac{2-\nu}{1-\nu} \left( \ln \frac{8R}{r_{\text{cut}}} - 2 \right) + \frac{1}{2} \right] + [\gamma_{\text{GSF}}(b_f + u_0) - \gamma_{\text{GSF}}(u_0)] \times \pi R^2 - b_f \tau_{\text{res}} \pi R^2, \quad (3)$$

where  $\gamma_{\text{GSF}}$  is a function describing the generalized stacking fault energy curve and  $u_0$  is the slip which occurs prior to dislocation nucleation when shear stress is applied.  $u_0$  is solved numerically from the condition  $\partial \gamma_{\text{GSF}}(u)/\partial u|_{u=u_0} = \tau_{\text{res}}$ . In this paper, we have chosen to use Eq. (3) to describe the energetics of a single homogeneous dislocation nucleation process. To obtain the energy barrier for dislocation nucleation at a given applied stress, we evaluate Eq. (3) on a fine grid in  $(b_f, R)$  space and then perform a numerical search for the saddle point of this two-dimensional function, which corresponds to the value of  $b_f$  that minimizes the maxima (i.e., the energy barrier for dislocation nucleation) along  $R$ .

In order to connect this to the observations of incipient plasticity during nanoindentation, we employ a similar statistical approach to that detailed in Refs. [44–46]. The local rate at which a single homogeneous dislocation nucleation event occurs per unit volume of material,  $\dot{n}$ , may be described by an Arrhenius rate equation of the form

$$\dot{n} = \eta \exp\left(-\frac{E_b}{k_B T}\right), \quad (4)$$

where  $E_b$  is the nucleation energy barrier now obtained from Eq. (3),  $k_B$  is the Boltzmann constant,  $T$  is the temperature, and  $\eta$  is a preexponential frequency factor. The global rate at which nucleation events occur,  $\dot{N}$ , is obtained by integrating the local nucleation rate over the volume of stressed material under the indenter ( $\Omega$ ),

$$\dot{N} = \iiint_{\Omega} \dot{n} d\Omega. \quad (5)$$

Full evaluation of this integral would require that we know the stress distribution under the indenter, which may not have

an analytical solution. As a simplification, we assume that the dislocation nucleation events occur within a small region directly beneath the indenter which experiences the maximum shear stress. Within the Hertzian framework for spherical contact [51], the volume  $\Omega$  is assumed to scale with the cube of the contact radius  $a$ ,

$$\Omega \approx K a^3 \approx \pi \left( \frac{3PR_i}{4E_R} \right), \quad (6)$$

where  $K$  is a proportionality constant on the order of  $\pi$ ,  $P$  is the applied load,  $R_i$  is the indenter radius, and  $E_R = \left( \frac{1-\nu_{\text{ind}}^2}{E_{\text{ind}}} + \frac{1-\nu_{\text{sp}}^2}{E_{\text{sp}}} \right)^{-1}$  is the reduced modulus of the indenter-specimen system. Within this small volume, the applied shear stress is assumed to be a constant, at a maximum value of

$$\tau_{\text{appl}} = \frac{0.31}{\pi} \left( \frac{6E_R^2}{R_i^2} \right)^{1/3} P^{1/3} = \alpha P^{1/3}, \quad (7)$$

where for simplicity of expression the constant terms have been collected into the parameter  $\alpha$ .

Now considering a series of indentations performed under nominally identical conditions, the cumulative probability for dislocation nucleation at time  $t$ ,  $F(t)$ , is then derived as follows. The rate of change of  $F(t)$  depends on the amount of unyielded sample and the rate at which dislocations nucleate within one of these unyielded samples,

$$\dot{F}(t) = [1 - F(t)] \dot{N}(t). \quad (8)$$

Integrating this yields the following expression for the cumulative probability function:

$$F(t) = 1 - \exp\left(-\int_0^t \dot{N}(t') dt'\right). \quad (9)$$

In the molecular dynamics simulations, indentation is carried out in displacement-controlled mode, meaning that the speed of the indenter,  $\dot{h}$ , is a constant. Assuming that the system exhibits a Hertzian elastic response where the load and displacement are related by

$$P = \frac{4}{3} E_R \sqrt{R_i h^3} = \beta h^{3/2}, \quad (10)$$

the loading rate can then be expressed as

$$\dot{P} = \frac{3}{2} \beta^{2/3} P^{1/3} \dot{h} = \frac{3}{2} \beta^{2/3} \frac{\tau_{\text{appl}}}{\alpha} \dot{h}. \quad (11)$$

Using the above expressions for the loading rate and the relationship between shear stress and load, we can rewrite the cumulative probability function as a function of the applied stress as

$$\begin{aligned} F(\tau_{\text{appl}}) &= 1 - \exp\left(-\int_0^{\tau_{\text{appl}}} \dot{N}(\tau') \frac{1}{P} \frac{dP}{d\tau'} d\tau'\right) = 1 - \exp\left(-\int_0^{\tau_{\text{appl}}} \pi a^3 \eta \exp\left(-\frac{E_b(\tau')}{kT}\right) \frac{2\alpha}{3\beta^{2/3} \tau' \dot{h}} \frac{3\tau'^2}{\alpha^3} d\tau'\right) \\ &= 1 - \exp\left(-\frac{\pi \eta}{\alpha^3} \left(\frac{3R_i}{4E_R}\right) \frac{2\alpha}{3\beta^{2/3} \dot{h}} \frac{3}{\alpha^3} \int_0^{\tau_{\text{appl}}} \exp\left(-\frac{E_b(\tau')}{kT}\right) \tau'^4 d\tau'\right) \\ &= 1 - \exp\left(-\frac{3\pi \eta R_i}{2\alpha^5 \beta^{2/3} \dot{h} E_R} \int_0^{\tau_{\text{appl}}} \exp\left(-\frac{E_b(\tau')}{kT}\right) \tau'^4 d\tau'\right). \end{aligned} \quad (12)$$

We demonstrate the application of this model, “model I,” to describe the statistics of incipient plasticity during nanoindentation of an fcc Cu single crystal in Sec. III B 1.

## 2. Model II: Complex concentrated alloy

The above model I assumes that the dislocation nucleates in a homogeneous material with uniform mechanical properties. However, this assumption may not be valid in complex concentrated alloys (CCAs), which typically comprise three to five elements in roughly equiatomic concentrations in a single solid solution. CCAs (also referred to as medium- or high-entropy alloys) are expected to exhibit some inhomogeneity in their properties due to the lack of long-range order in their chemical structure, although some degree of short-range order (SRO) may exist. In this section, we modify model I to account for unequal nucleation rates within a CCA sample due to the spatially varying generalized stacking fault energy (GSFE) surface.

First, we construct a simple model by assuming that a dislocation loop starts nucleating in a region of the material with some given local GSFE. Outside of this region of radius  $r_0$ , the GSFE approaches the macroscopic average for the system. This transition from a local GSFE  $\gamma_{\text{GSF}}^{\text{loc}}$  to average GSFE  $\gamma_{\text{GSF}}^{\text{av}}$  is described by a simple logistic (smooth step) function:

$$\gamma_{\text{GSF}}(r) = \frac{\gamma_{\text{GSF}}^{\text{av}} - \gamma_{\text{GSF}}^{\text{loc}}}{1 + \exp(-k(r - r_0))} + \gamma_{\text{GSF}}^{\text{loc}}, \quad (13)$$

where  $r$  is the distance from the center of the “local region” where the dislocation begins nucleating and the parameter  $k$  (we used  $k = 5 \times 10^{10}$ ) controls the steepness of the transition.

The local (average) GSFE function  $\gamma_{\text{GSF}}(u)$  is approximated using a simple analytic expression parametrized by the local (average) intrinsic and unstable stacking fault energies,

$$\begin{aligned} \gamma_{\text{GSF}}(u) = & \frac{1}{2} \left( \gamma_{\text{USF}} - \frac{\gamma_{\text{ISF}}}{2} \right) \left( 1 - \cos \left( \frac{2\pi u}{b} \right) \right) \\ & + \gamma_{\text{ISF}} \left( -2 \left( \frac{u}{b} \right)^3 + 3 \left( \frac{u}{b} \right)^2 \right), \end{aligned} \quad (14)$$

where  $u$  is the slip vector and  $b$  is the Burgers vector.

Hence we replace the one-dimensional  $\gamma_{\text{GSF}}(u)$  function in Eq. (3) by a two-dimensional  $\gamma_{\text{GSF}}(u, R)$  function to represent the spatially varying GSFE landscape encountered by the dislocation loop as it expands (i.e., as its radius  $R$  increases). As before, we reevaluate Eq. (3) with this modified  $\gamma_{\text{GSF}}(u, R)$  function on a fine grid in  $(b_f, R)$  space and then perform a numerical search for the saddle point of this two-dimensional function, which gives the local energy barrier for dislocation nucleation. Based on this model, the energy barrier and hence the local nucleation rate clearly depend on both the value of the local GSFE and the size of the local region.

The second modification we make to the model is to weight the local nucleation rates based on the volume fraction of the material with a given  $\gamma_{\text{GSF}}^{\text{loc}}$  (i.e., a given combination of  $\gamma_{\text{ISF}}^{\text{loc}}$  and  $\gamma_{\text{USF}}^{\text{loc}}$ ). As shown in Fig. 1(a), the distributions of both  $\gamma_{\text{ISF}}^{\text{loc}}$  and  $\gamma_{\text{USF}}^{\text{loc}}$  in a CrCoNi CCA sample may be approximated by normal distributions with mean values  $\gamma_{\text{ISF}}^{\text{av}}$  and  $\gamma_{\text{USF}}^{\text{av}}$  and standard deviations  $\sigma_{\text{ISF}}$  and  $\sigma_{\text{USF}}$ .  $\gamma_{\text{ISF}}^{\text{loc}}$  and  $\gamma_{\text{USF}}^{\text{loc}}$  were not found

to be significantly correlated; hence for simplicity they are treated as two independent distributions. Then, the weighted local nucleation rate can be expressed as

$$\begin{aligned} \dot{n}_{\text{CCA}} = & \eta A_{\text{ISF}} A_{\text{USF}} \sum_{\gamma_{\text{ISF}}^{\text{loc}}} \sum_{\gamma_{\text{USF}}^{\text{loc}}} \left\{ \exp \left( - \frac{E_b(\tau_{\text{res}}, \gamma_{\text{ISF}}^{\text{loc}}, \gamma_{\text{USF}}^{\text{loc}})}{kT} \right) \right. \\ & \times \exp \left( - \frac{1}{2} \left( \frac{\gamma_{\text{ISF}}^{\text{loc}} - \gamma_{\text{ISF}}^{\text{av}}}{\sigma_{\text{ISF}}} \right)^2 \right) \\ & \left. \times \exp \left( - \frac{1}{2} \left( \frac{\gamma_{\text{USF}}^{\text{loc}} - \gamma_{\text{USF}}^{\text{av}}}{\sigma_{\text{USF}}} \right)^2 \right) \right\}, \end{aligned} \quad (15)$$

where  $A_{\text{ISF}}$  and  $A_{\text{USF}}$  are the normalization constants of the respective normal distributions.

The weighted  $\dot{n}$  defined in Eq. (15) may be thought of as a spatially averaged local nucleation rate. The constant  $\dot{n}$  in Eq. (4) is replaced by the weighted  $\dot{n}$ , and the rest of the statistical model is constructed as before. We demonstrate the application of this model, “model II,” to describe the statistics of incipient plasticity during nanoindentation of CrCoNi CCA samples in Sec. III B 2.

## III. RESULTS

### A. Atomistic mechanism of dislocation nucleation

Four material systems are studied in detail in this paper including single-crystal Cu, random solid solution (RSS) CrCoNi, and CrCoNi alloys with low and high degrees of short-range order (SRO). The low- and high-SRO samples were obtained by performing Monte Carlo simulations at 900 and 600 K, respectively. The CoCr order parameter  $\alpha_{\text{CoCr}}$  is  $-0.36$  for the low-SRO sample and  $-0.58$  for the high-SRO sample. Figure 1(a) shows the microstructure of CrCoNi samples with different degrees of SRO and the distributions of the intrinsic stacking fault energy (ISFE) and USFE. As discussed in previous studies [17], we can observe a higher tendency for Ni segregation and CrCo clustering with increasing SRO, and the distributions of ISFE and USFE were both shifted to higher values. The increase in ISFE and USFE with degree of SRO is understood as greater energy is required to disrupt the more energetically stable SRO configurations.

Negative local ISFEs are predicted primarily in the RSS sample, in line with *ab initio* predictions in CrCoNi and other CCAs, and have been shown to correspond to structures in which hcp stacking is (at least locally) more energetically stable than fcc [8,52–58]. Meanwhile, experimental estimates of ISFEs are always positive [5,59,60]. Various reasons for the discrepancies have been suggested, including that experimental samples contain SRO [8], SFEs have strong temperature dependence [55], or the elasticity theory models underlying experimental estimates of SFE neglect solute and dislocation interactions [58] or lattice friction forces [61], although no consensus has been reached. Hence it is difficult to know the “true” distribution of ISFEs in a given sample, and we cannot discount that there may be regions with negative local ISFE, even in a sample with positive average ISFE. However, even in regions of negative ISFE, this does not mean that dislocations can nucleate spontaneously since the USFE is still positive, and the same physics governing dislocation nucleation should

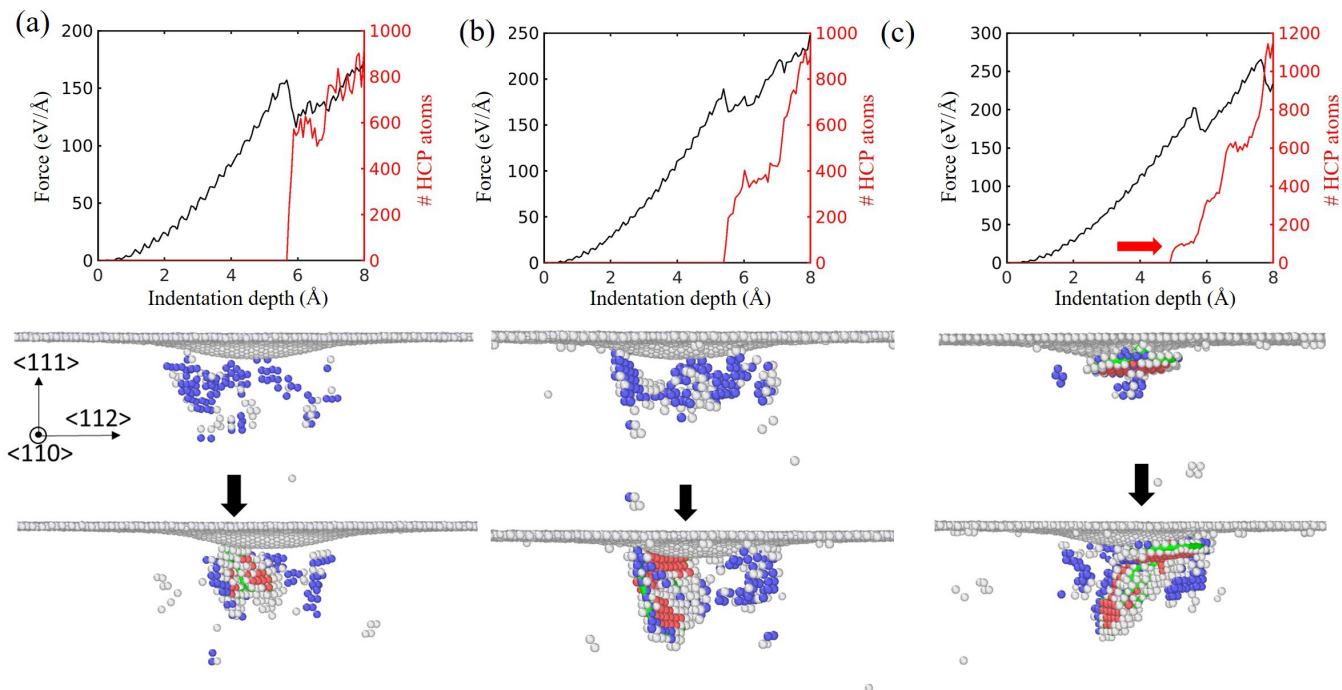


FIG. 2. Typical dislocation nucleation process in Cu (a) and two CrCoNi samples [(b) and (c)]. The fcc atoms are removed from the system, and the remaining atoms are colored by their structure types. Blue atoms have bcc structure, red atoms have hcp structure, and white atoms have unknown coordination structure.

still apply. We consider different sets of samples ranging from RSS to low SRO to high SRO to demonstrate that our model is generally applicable to systems with both positive and/or negative ISFEs.

Nanoindentation tests were performed on the four material systems to obtain the distribution of critical pop-in strength using the setup shown in Fig. 1(b). Figure 1(c) shows a typical indentation force-depth curve from MD simulation. At the initial stage of the indentation, the material undergoes elastic deformation which can be described very well by the Hertzian elastic response [51] [Eq. (10)]. We obtained the reduced modulus  $E_R$  for each indentation test by fitting the force-depth curve before the pop-in event to this expression, and the averaged values are listed in Tables S1–S3 in the Supplemental Material [62]. The pop-in event is indicated by the sudden load drop in the force-indentation depth curve which coincides with the rapid increase in the number of “hcp-like” atoms found in stacking faults generated by the nucleation of partial dislocations.

Figure 2 shows the typical dislocation nucleation process in pure Cu and CrCoNi alloys. In all the indented Cu samples, Shockley partial dislocations nucleated from embryos with distorted lattice structure under the indenter as shown in Fig. 2(a). The nucleated dislocation loop can propagate along the (111) plane tilted to the indentation surface and immediately induce the load drop. For the CrCoNi alloys, two distinct nucleations are observed regardless of the degree of SRO of the samples. The first type as shown in Fig. 2(b) is similar to the dislocation nucleation process in pure Cu where the pop-in event corresponds to nucleation of the first dislocation loop. The other dislocation nucleation pattern observed in CrCoNi alloys involves the nucleation of a dislocation loop

that lies on the (111) plane parallel to the indentation surface as shown in Fig. 2(c). This type of dislocation loop has a typical diameter of around 2 nm in current MD simulations (Fig. S2) and does not expand further. With further loading, new dislocation loops subsequently nucleate near the existing loop and propagate on inclined (111) planes, which induces the pop-in event.

## B. Theoretical modeling of the pop-in load distribution

### 1. fcc Cu

We identify the loads corresponding to the first pop-in events from the load-displacement curves of each nanoindentation simulation and plot them as a cumulative probability distribution in Fig. 3(a). These data can also be converted into the applied shear stress at first pop-in, binned into a probability density histogram, and smoothed using a Gaussian kernel density estimate (KDE), as depicted in Fig. 3(b). Fluctuations in the statistical distribution—which are amplified in the probability density representation—may arise due to the relatively small data sets; hence we caution against overinterpreting them. In the following discussion, we focus mainly on fitting the overall shape of the cumulative probability distributions predicted by the model to that obtained from the corresponding MD simulations.

In the case of pure fcc Cu, we apply model I above, with the following material and indentation parameters: material properties calculated using the Mishin EAM potential for Cu [48] (see also Table S1)  $\mu = 39$  GPa,  $\nu = 0.41$ ,  $\gamma_{\text{ISF}} = 44$  mJ/m<sup>2</sup>, and  $\gamma_{\text{USF}} = 170$  mJ/m<sup>2</sup>, reduced modulus of indenter-specimen system  $E_R \approx 171.1$  GPa as estimated from the elastic part of the force-displacement curves,

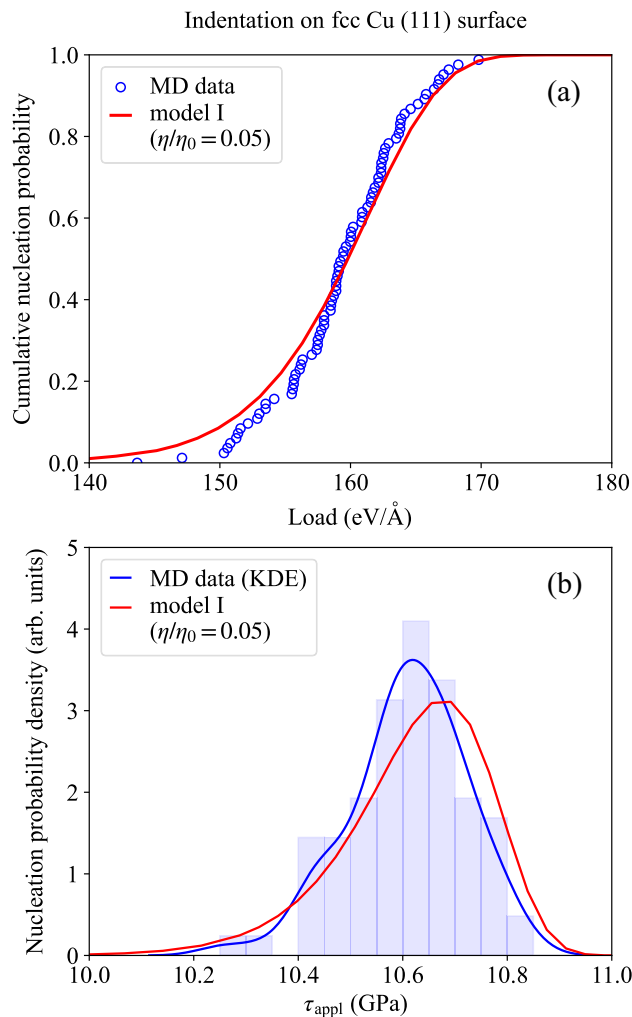


FIG. 3. Comparison between our theoretical model (red curves) and MD statistics of dislocation nucleation during nanoindentation of the fcc Cu (111) surface (blue symbols or curve). The model shows good agreement with the MD data both (a) when visualized in terms of the cumulative nucleation probability and (b) when visualized in terms of its derivative, the nucleation probability density.

indenter radius  $R_i = 6$  nm, indenter speed  $\dot{h} = 3.5$  m/s, and temperature  $T = 300$  K.

As done by Schuh, Lund, and Mason [44–46], we treat the preexponential frequency factor  $\eta$  as a fitting parameter for the model. For a simple atomic process (e.g., vacancy hop), the frequency prefactor of the rate equation may be approximated from the atomic vibration frequency and the atomic density, i.e.,  $\eta_0 \approx 10^{13} \text{ s}^{-1} \times (a_0^3/4)^{-1} \text{ m}^{-3} \approx 10^{42} \text{ s}^{-1} \text{ m}^{-3}$ . For a complex process such as dislocation loop formation, this frequency prefactor is difficult to define but is expected to be of a comparable order of magnitude but smaller than  $\eta_0$  as it involves the simultaneous activation of multiple atoms.

The result from our theoretical model is plotted in red in Figs. 3(a) and 3(b). A fitting parameter value of  $\eta \approx 5 \times 10^{40} \text{ s}^{-1} \text{ m}^{-3}$  gives a good fit between the model and MD results, as shown. Based on the reasoning above, this value for  $\eta$  appears to be physically reasonable, and the good

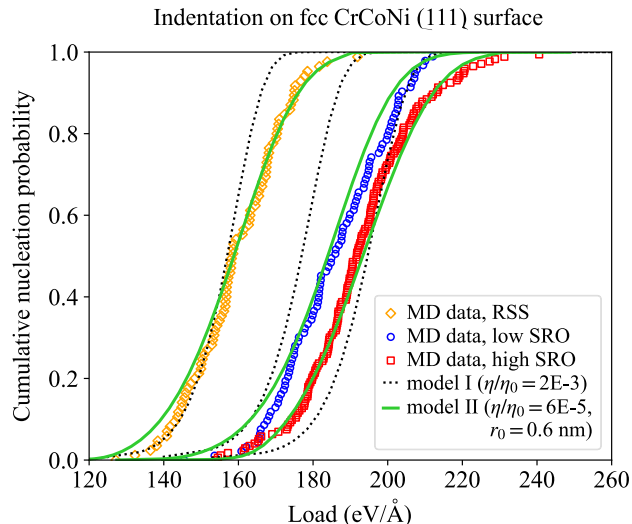


FIG. 4. Comparison between two different theoretical models and MD statistics of dislocation nucleation during nanoindentation of the fcc CrCoNi (111) surface. The black dotted lines indicate the prediction of model I, which assumes a uniform average SFE, while the green solid lines indicate the prediction of the modified model II, which accounts for a distribution of ISFE and USFE. In the legend, 2E-3 and 6E-5 mean  $2 \times 10^{-3}$  and  $6 \times 10^{-5}$ , respectively.

fit between the model and the MD data validates our approach to constructing the model and the choice of model parameters.

## 2. fcc CCA CrCoNi

Figure 4 shows the cumulative probability distributions of the first pop-in load during nanoindentation simulations on three types of CrCoNi samples: random solid solution (RSS), low degree of short-range order (low SRO), and high degree of short-range order (high SRO). As expected, the samples with higher SRO are found to exhibit higher yield strength, as evidenced by the rightward shift of the cumulative probability distribution curves. Meanwhile, the overall shapes of the curves appear similar across all three sets of samples. These are the key features that we aim to reproduce using our model.

We apply the modified model II, which accounts for a spatially varying distribution of local GSFE, and carry out a similar procedure to that followed before to fit the model prediction to the corresponding MD data. The material parameters including the means and standard deviations of the ISFE and USFE distributions are listed in Table S2. While there are slight differences in the elastic constants across the CrCoNi samples, the largest and most significant differences are in the means of the ISFE (and USFE) distributions, which increase from  $-16$  (310) to  $34$  (335) to  $70$  (348)  $\text{mJ/m}^2$  with increasing degree of SRO, while the widths of the distributions remain similar. The indentation parameters are the same as those used for the nanoindentation of fcc Cu ( $R_i = 6$  nm,  $\dot{h} = 3.5$  m/s,  $T = 300$  K).

In addition to varying the parameter  $\eta$ , this time we also evaluate the model II for different values of  $r_0$  (size of local region) to find a good fit to the MD data. The dependence

of the model results on  $r_0$  is illustrated in Fig. S3. When evaluated with  $r_0$  less than  $\approx 0.3$  nm, model II approaches model I, i.e., the uniform SFE case, as the dislocation loop is unable to fully nucleate within the small local region; hence the nucleation barrier is determined by the average GSFE outside of the local region. On the other hand, when  $r_0$  is greater than  $\approx 0.6$  nm, the model also converges as the dislocation loop can now almost always fully nucleate within the local region. The model is very sensitive to  $r_0$  in the intermediate range, where depending on the combination of local GSFE and applied stress, the critical loop size  $r_{\text{crit}}$  may sometimes fall within  $r_0$  and sometimes exceed  $r_0$ .

The comparison between our models and the MD data is plotted in Fig. 4, showing that our model II reproduces the key trends and features in the MD data well. Each set of CrCoNi samples (RSS, low SRO, and high SRO) was independently fitted to a corresponding model, and interestingly, we found that similar values of  $\eta \approx 6 \times 10^{37} \text{ s}^{-1} \text{ m}^{-3}$  and  $r_0 \approx 0.6$  nm yielded good fits in each case. For comparison, the results from model I (evaluated with  $\eta \approx 2 \times 10^{39} \text{ s}^{-1} \text{ m}^{-3}$ ) are also shown, but it is clear that the simple uniform SFE model is not able to capture the width of the distributions or the relative positions of the curves as well as the modified model II. This demonstrates that our simplified model accounting for the spatial variation of the GSFE surface is able to capture the key differences in the statistics of incipient plasticity during nanoindentation of complex concentrated alloys versus conventional metals. Small discrepancies mostly at low loads may be due to the nucleation of dislocations prior to first pop-in as shown in Fig. 2(c), which effectively releases the local stress concentration and increases the pop-in load for subsequent dislocation nucleation.

#### IV. DISCUSSION

This work connects a material's fundamental properties derived from atomistic simulations with statistical analysis of its mechanical response, specifically applied to model incipient plasticity during nanoindentation. In the original formulation and subsequent applications of the statistical model, it was fit to experimental data for which the underlying nucleation mechanism(s) were not known and could only be inferred from the model fitting parameters. Meanwhile, MD simulation studies of nanoindentation tend to focus on details of a few individual dislocation nucleation events, which while useful for providing atomistic details of the process, may not capture the whole picture of an inherently statistical process as presented in this paper. By combining statistical analysis with a physically informed model describing the underlying mechanism and validating this approach against statistical data obtained from MD simulations, we directly link the material's fundamental properties at an atomistic scale to the observable statistical behavior of a macroscopic sample under nanoindentation. By replacing the empirical expression for the activation energy for nucleation assumed in previous works with one derived from elasticity theory and informed by fundamental material properties (e.g., GSFE, shear modulus, Poisson ratio), we also reduce the reliance of the statistical model on empirical parameters. By constructing the model

this way, it is relatively straightforward to extend our model to explicitly account for the spatial variation of the GSFE in CCAs and predict the effect on the overall statistics of incipient plasticity in good agreement with MD simulations.

Incipient plasticity in CCAs differs from that in the pure metals because of their unique microstructural features including chemical inhomogeneity, SRO, and residual stress. Unlike the homogenous pure metal, material properties of CCAs such as SFE demonstrate large spatial variations, which can induce unexpected mechanical behavior such as dislocation self-pinning and enhanced strength [17,63]. The direct consequence of this spatial variation in our nanoindentation simulations is the widening of the statistical distribution of the pop-in force of CrCoNi samples compared with pure Cu. Dislocation nucleation under the indenter is governed by the combined effects of the stress field and the local material properties. Thus the favorable nucleation sites in CrCoNi samples can deviate from the site with the maximum shear stress [Figs. S1(c) and S1(f)], and the distribution of the pop-in force shows larger scatter. Cr-rich regions [Figs. S1(b) and S1(e)] are observed to be the favorable nucleation sites, which is attributed to the weak Cr-Cr bonding [25]. With increased SRO in the sample, the averaged values of the SFE and USFE both increase due to the extra energy required to break the local ordered clusters, which increases the overall pop-in forces.

In order to obtain the local ISFE and USFE distributions as inputs to our model, we averaged them over cross-sectional areas of  $1.6 \times 1.6$  nm in this paper. This choice of averaging cross section may be thought of as a "spatial resolution" through which the GSFE surface is viewed. In the extreme, one may consider fluctuations of the GSFE surface which exist on an atomic length scale; however, such fluctuations may not ultimately have a significant impact on the material behavior of interest. For the purposes of our model, the relevant length scale which we are interested in is the length scale over which the dislocation loop interacts with the GSFE landscape as it expands. The local SFE averaged over this area determines the average energy barrier for loop nucleation, and hence the nucleation probability. Hence the local SFE distributions which are input into the model as weighting functions should reflect a spatial resolution roughly corresponding to the critical loop diameter for dislocation nucleation, which is on the order of 1–2 nm under the given conditions. This justifies our choice of averaging cross-sectional area of  $1.6 \times 1.6$  nm employed in this paper to obtain the local ISFE and USFE distributions, which ensures that the weighting in the model reflects the likelihood of encountering local regions of a critical size sufficient for nucleation. The value of  $r_0$  which emerges from the model fitting is also consistent with this length scale, which further supports the argument for the appropriate choice of spatial resolution of the GSFE surface and its physical origin.

While SRO has a general strengthening effect, we note that the overall widths of the cumulative probability distribution curves from our MD simulations look similar across the three CrCoNi samples considered in this paper. The rightward shift of the curves corresponding to higher pop-in loads in samples with higher SRO can be clearly understood as a higher energy barrier (USFE) has to be overcome to initiate slip in a structure that contains energetically favorable SRO. However, in our

simulations, the degree of SRO does not appear to have a significant impact on the shape of the statistical distribution of pop-in load. Although the atomic-level fluctuations in the GSFE surface may differ between our RSS and SRO samples, when averaged over a length scale of  $\approx 1.6$  nm, the distributions of locally averaged ISFE and USFE have shifted mean values but small deviations in the overall shape across all samples (Fig. 1), thus giving rise to the similar overall shapes of the cumulative probability distribution curves. This trend suggests that the nucleation statistics are not sensitive to differences in the fluctuations at the atomic level; otherwise, we might expect to see clear differences in the shape of the distributions when comparing samples without and with SRO, e.g., multimodality corresponding to nucleation from different SRO domains, which was not evident in our simulations.

For further comparison, an additional system, RSS  $\text{Cu}_{60}\text{Ni}_{40}$ , which has narrower SFE distributions was also computed, and the data and model fit are shown in the Supplemental Material, Table S3 and Fig. S4(b). A comparison across all three material systems clearly shows that the width of the statistical distribution of pop-in loads is largely influenced by the width of the local SFE distributions, which is determined more by the nominal chemical composition than the degree of SRO, especially since the typical SRO domains in such alloys tend to be on this length scale or smaller [5]. In systems where the SRO length scale is larger, or the critical length scale of the underlying mechanism is comparatively smaller, we might expect the degree of SRO to have a greater effect on the shape or width of the statistical distribution of pop-in loads.

A new dislocation nucleation pathway can also be triggered in CCAs due to the interaction of stress field and material inhomogeneity as shown in Fig. 2. Shear stress [Fig. S2(b)] under the indenter is sufficient to facilitate the nucleation of the dislocation loop on the parallel plane to the surface when the local chemical environment of the parallel plane is easier for dislocation nucleation than that of the inclined plane. A Shockley dislocation loop first nucleates from the Cr-rich region and grows to a steady state with a diameter of around 2 nm in our simulations [Fig. S2(c)]. Further expansion of the dislocation loop is not observed with increased indentation depth in our simulation, given the lack of driving force away from the indenter. Instead, new dislocation loops nucleate on the inclined planes near the parallel loop and induce the sudden load drop. The nucleation of parallel loops prior to the pop-in event can release the local stress concentration and effectively increase the pop-in force. This is not considered in our current model and could be a source of some discrepancies between the model and data, especially at low loads.

In our models, the parameter  $\eta$  appears as the prefactor in the Arrhenius rate equation governing the dislocation loop nucleation. As discussed earlier in Sec. III B 1, the exact value of this prefactor for a complex process such as dislocation loop formation is difficult to define. Furthermore, as the main fitting parameter in our models,  $\eta$  effectively encompasses other approximations as well, e.g., indenter stress distribution; hence it is not possible for us to ascribe a definitive meaning to the value of this parameter. That said, we do believe that this parameter should be related to physical properties of the system, albeit not in a straightforward manner. Our obser-

vation that a similar value of this fitting parameter appears to fit our data for CrCoNi across the three types of samples suggests that it is not arbitrary and that it is related to some fundamental material properties which are seemingly not very sensitive to the degree of SRO. We note that Schuh, Lund, and Mason [44–46] did not attempt to justify the value of this parameter in their works either, but simply treated it as a fitting parameter similar to what we have done.

Given its simplicity, there are certainly some aspects of the nanoindentation process which are not fully captured by our current model. One simplifying approximation that we made was to assume that the homogeneous dislocation nucleation events occur only within a small spherical region directly beneath the indenter which experiences the maximum shear stress. Mason, Lund, and Schuh [46] found that their simpler analytical model using this same simplifying assumption loses little accuracy when compared with a more mathematically complex numerical model incorporating the entire stress field within the Hertzian framework. Therefore we have also adopted this approximation in our models.

Direct comparison of our model with experiments is challenging due to the differences in length scale and hence dominant mechanisms at play. In nanoindentation experiments, the indenter tip tends to be at least hundreds of nanometers in radius, which makes it difficult to observe homogeneous dislocation nucleation, as it is more favorable for dislocations to nucleate heterogeneously at defects which are present at that length scale. Indeed, the relatively lower pop-in stresses ( $< 10$  GPa) and small activation volumes (0.5–3 atomic volumes) observed in nanoindentation experiments on CCAs suggest heterogeneous dislocation nucleation as the dominant mechanism in these experiments [28–30]. However, we believe that the insight that the spatial variation in the SFE leads to the broadening of the statistical distribution of the pop-in force during homogeneous dislocation nucleation also applies to other dislocation nucleation mechanisms. For example, it may explain the broader distribution of pop-in loads observed by Mridha *et al.* in CrCoNi compared with Ni [29]. The broadening of these distributions may also support Zhao *et al.*'s suggestion that the bimodality observed in their pop-in strength distributions may be due to overlap in the strength distributions associated with different mechanisms in CCAs [30].

## V. CONCLUSION

In this paper, we have combined elasticity theory and statistical modeling into a single theoretical model which connects a material's fundamental properties to the statistics of incipient plasticity during nanoindentation, and validated the model against statistical data obtained from MD simulations on fcc Cu and CrCoNi alloys. By accounting for the spatially varying local ISFE and USFE in CCAs, our theoretical model captures the key features of the statistics of incipient plasticity in CCAs with varying degrees of local short-range order. The spatial variation of material properties in CCAs widens the statistical distribution of the pop-in load during nanoindentation and triggers new dislocation nucleation activities. Our work shows that the length scale over which the local fluctuations in material properties affect the statistics of incipient plasticity

in CCAs is determined by the critical length scale of the underlying mechanism, in this case, the critical loop size during homogeneous dislocation nucleation. The insights from our work on dislocation nucleation complement previous studies which have demonstrated the effect of local fluctuations in material properties and short-range order on dislocation glide behavior in CCAs, which leads to wavy dislocation lines and a nanoscale detrapping mechanism [16,17,22,27]. We expect that the spatial variation of other material properties, including solution energy, grain boundary energy, surface energy, etc., would also affect other deformation mechanisms in CCAs and should be accounted for accordingly when developing physics-based models for such systems.

## ACKNOWLEDGMENTS

We thank Prof. Upadrasta Ramamurty and Dr. Yakai Zhao from Nanyang Technological University for discussions about nanoindentation of CCAs. A.M.Z.T. was supported by the Agency for Science, Technology and Research (A\*STAR) through the Structural Metals and Alloys Program (Grant No. A18B1b0061). Z.L. and H.G. were supported by a research startup grant from Nanyang Technological University (Grant No. 002479-00001) and A\*STAR. The computational work for this paper was partially performed on resources of the National Supercomputing Centre (NSCC), Singapore [64], as well as the supercomputer Fugaku provided by the RIKEN Center for Computational Science.

- 
- [1] M.-H. Tsai and J.-W. Yeh, *Mater. Res. Lett.* **2**, 107 (2014).  
 [2] D. B. Miracle and O. N. Senkov, *Acta Mater.* **122**, 448 (2017).  
 [3] E. P. George, W. A. Curtin, and C. C. Tasan, *Acta Mater.* **188**, 435 (2020).  
 [4] J.-W. Yeh, S.-K. Chen, S.-J. Lin, J.-Y. Gan, T.-S. Chin, T.-T. Shun, C.-H. Tsau, and S.-Y. Chang, *Adv. Eng. Mater.* **6**, 299 (2004).  
 [5] R. Zhang, S. Zhao, J. Ding, Y. Chong, T. Jia, C. Ophus, M. Asta, R. O. Ritchie, and A. M. Minor, *Nature (London)* **581**, 283 (2020).  
 [6] X. Chen, Q. Wang, Z. Cheng, M. Zhu, H. Zhou, P. Jiang, L. Zhou, Q. Xue, F. Yuan, J. Zhu, X. Wu, and E. Ma, *Nature (London)* **592**, 712 (2021).  
 [7] A. Tamm, A. Aabloo, M. Klintonberg, M. Stocks, and A. Caro, *Acta Mater.* **99**, 307 (2015).  
 [8] J. Ding, Q. Yu, M. Asta, and R. O. Ritchie, *Proc. Natl. Acad. Sci. USA* **115**, 8919 (2018).  
 [9] F. Walsh, M. Asta, and R. O. Ritchie, *Proc. Natl. Acad. Sci. USA* **118**, e2020540118 (2021).  
 [10] B. Cantor, I. Chang, P. Knight, and A. Vincent, *Mater. Sci. Eng. A* **375-377**, 213 (2004).  
 [11] B. Gludovatz, A. Hohenwarter, D. Catoor, E. H. Chang, E. P. George, and R. O. Ritchie, *Science* **345**, 1153 (2014).  
 [12] B. Gludovatz, A. Hohenwarter, K. V. S. Thurston, H. Bei, Z. Wu, E. P. George, and R. O. Ritchie, *Nat. Commun.* **7**, 10602 (2016).  
 [13] H. Luo, Z. Li, and D. Raabe, *Sci. Rep.* **7**, 9892 (2017).  
 [14] H. Luo, W. Lu, X. Fang, D. Ponge, Z. Li, and D. Raabe, *Mater. Today* **21**, 1003 (2018).  
 [15] Z. H. Aitken, V. Sorkin, and Y.-W. Zhang, *J. Mater. Res.* **34**, 1509 (2019).  
 [16] E. Ma, *Scr. Mater.* **181**, 127 (2020).  
 [17] Q.-J. Li, H. Sheng, and E. Ma, *Nat. Commun.* **10**, 3563 (2019).  
 [18] Z. F. Liu, N. Tian, Y. G. Tong, Y. L. Hu, D. Y. Deng, M. J. Zhang, Z. H. Cai, and J. Liu, *Crystals* **12**, 753 (2022).  
 [19] A. Gupta, W.-R. Jian, S. Xu, I. J. Beyerlein, and G. J. Tucker, *Int. J. Plast.* **159**, 103442 (2022).  
 [20] S. Xu, Y. Su, W.-R. Jian, and I. J. Beyerlein, *Acta Mater.* **202**, 68 (2021).  
 [21] S. Yin, Y. Zuo, A. Abu-Odeh, H. Zheng, X.-G. Li, J. Ding, S. P. Ong, M. Asta, and R. O. Ritchie, *Nat. Commun.* **12**, 4873 (2021).  
 [22] Y. Zeng, X. Cai, and M. Koslowski, *Acta Mater.* **164**, 1 (2019).  
 [23] L. Zhang, Y. Xiang, J. Han, and D. J. Srolovitz, *Acta Mater.* **166**, 424 (2019).  
 [24] C. Li, F. Cao, Y. Chen, H. Wang, and L. Dai, *Metals* **12**, 1757 (2022).  
 [25] F.-H. Cao, Y.-J. Wang, and L.-H. Dai, *Acta Mater.* **194**, 283 (2020).  
 [26] J. Xiao, N. Wu, O. Ojo, and C. Deng, *Materialia* **12**, 100749 (2020).  
 [27] W.-R. Jian, Z. Xie, S. Xu, Y. Su, X. Yao, and I. J. Beyerlein, *Acta Mater.* **199**, 352 (2020).  
 [28] C. Zhu, Z. Lu, and T. Nieh, *Acta Mater.* **61**, 2993 (2013).  
 [29] S. Mridha, M. Sadeghilaridjani, and S. Mukherjee, *Metals* **9**, 263 (2019).  
 [30] Y. Zhao, J.-M. Park, J.-I. Jang, and U. Ramamurty, *Acta Mater.* **202**, 124 (2021).  
 [31] J. Li, K. J. Van Vliet, T. Zhu, S. Yip, and S. Suresh, *Nature (London)* **418**, 307 (2002).  
 [32] Y. Lee, J. Y. Park, S. Y. Kim, S. Jun, and S. Im, *Mech. Mater.* **37**, 1035 (2005).  
 [33] G. Ziegenhain, A. Hartmaier, and H. M. Urbassek, *J. Mech. Phys. Solids* **57**, 1514 (2009).  
 [34] G. Ziegenhain, H. M. Urbassek, and A. Hartmaier, *J. Appl. Phys.* **107**, 061807 (2010).  
 [35] K. Xiong and J. Gu, *Intermetallics* **67**, 111 (2015).  
 [36] K. Xiong, H. Lu, and J. Gu, *Comput. Mater. Sci.* **115**, 214 (2016).  
 [37] X. Fan, Z. Rui, H. Cao, R. Fu, R. Feng, and C. Yan, *Materials* **12**, 770 (2019).  
 [38] I. A. Alhafez, C. J. Ruestes, E. M. Bringa, and H. M. Urbassek, *J. Alloys Compd.* **803**, 618 (2019).  
 [39] Y. Tian, Q. Fang, and J. Li, *Nanotechnology* **31**, 465701 (2020).  
 [40] Y. Qiu, Y. Qi, H. Zheng, T. He, and M. Feng, *J. Appl. Phys.* **130**, 125102 (2021).  
 [41] S. Shuang, S. Lu, B. Zhang, C. Bao, Q. Kan, G. Kang, and X. Zhang, *Comput. Mater. Sci.* **195**, 110495 (2021).  
 [42] A. Mu, Y. Han, X. Song, Y. Dong, Y. Hong, G. Zhang, and R. Hua, *Mater. Sci. Technol.* **37**, 202 (2021).  
 [43] D. Hua, Q. Xia, W. Wang, Q. Zhou, S. Li, D. Qian, J. Shi, and H. Wang, *Int. J. Plast.* **142**, 102997 (2021).  
 [44] C. A. Schuh and A. C. Lund, *J. Mater. Res.* **19**, 2152 (2004).  
 [45] C. A. Schuh, J. K. Mason, and A. C. Lund, *Nat. Mater.* **4**, 617 (2005).

- [46] J. K. Mason, A. C. Lund, and C. A. Schuh, *Phys. Rev. B* **73**, 054102 (2006).
- [47] S. Plimpton, *J. Comput. Phys.* **117**, 1 (1995).
- [48] Y. Mishin, M. J. Mehl, D. A. Papaconstantopoulos, A. F. Voter, and J. D. Kress, *Phys. Rev. B* **63**, 224106 (2001).
- [49] B. Sadigh, P. Erhart, A. Stukowski, A. Caro, E. Martinez, and L. Zepeda-Ruiz, *Phys. Rev. B* **85**, 184203 (2012).
- [50] S. Aubry, K. Kang, S. Ryu, and W. Cai, *Scr. Mater.* **64**, 1043 (2011).
- [51] K. L. Johnson, *Contact Mechanics* (Cambridge University Press, Cambridge, 1985).
- [52] H. Huang, X. Li, Z. Dong, W. Li, S. Huang, D. Meng, X. Lai, T. Liu, S. Zhu, and L. Vitos, *Acta Mater.* **149**, 388 (2018).
- [53] Z. Zhang, H. Sheng, Z. Wang, B. Gludovatz, Z. Zhang, E. P. George, Q. Yu, S. X. Mao, and R. O. Ritchie, *Nat. Commun.* **8**, 14390 (2017).
- [54] Z. Pei, S. Zhang, Y. Lei, F. Zhang, and M. Chen, *Proc. Natl. Acad. Sci. USA* **118**, e2114167118 (2021).
- [55] S. Zhao, G. M. Stocks, and Y. Zhang, *Acta Mater.* **134**, 334 (2017).
- [56] Y. H. Zhang, Y. Zhuang, A. Hu, J. J. Kai, and C. T. Liu, *Scr. Mater.* **130**, 96 (2017).
- [57] C. Niu, C. R. LaRosa, J. Miao, M. J. Mills, and M. Ghazisaeidi, *Nat. Commun.* **9**, 1363 (2018).
- [58] M. Shih, J. Miao, M. Mills, and M. Ghazisaeidi, *Nat. Commun.* **12**, 3590 (2021).
- [59] G. Laplanche, A. Kostka, C. Reinhart, J. Hunfeld, G. Eggeler, and E. P. George, *Acta Mater.* **128**, 292 (2017).
- [60] S. F. Liu, Y. Wu, H. T. Wang, J. Y. He, J. B. Liu, C. X. Chen, X. J. Liu, H. Wang, and Z. P. Lu, *Intermetallics* **93**, 269 (2018).
- [61] X. Sun, S. Lu, R. Xie, X. An, W. Li, T. Zhang, C. Liang, X. Ding, Y. Wang, H. Zhang, and L. Vitos, *Mater. Des.* **199**, 109396 (2021).
- [62] See Supplemental Material at <http://link.aps.org/supplemental/10.1103/PhysRevMaterials.7.053601> for additional figures and tables.
- [63] J. Yan, S. Yin, M. Asta, R. O. Ritchie, J. Ding, and Q. Yu, *Nat. Commun.* **13**, 2789 (2022).
- [64] <https://www.nscg.sg>.